

## Noninvasive fluence rate mapping in living tissues using magnetic resonance thermometry

Tom J. L. Schreurs  
Robbert van Gorkum  
Xu U. Zhang  
Dirk J. Faber  
Ton G. van Leeuwen  
Klaas Nicolay  
Gustav J. Strijkers

# Noninvasive fluence rate mapping in living tissues using magnetic resonance thermometry

Tom J. L. Schreurs,<sup>a,\*</sup> Robbert van Gorkum,<sup>b</sup> Xu U. Zhang,<sup>c</sup> Dirk J. Faber,<sup>c</sup> Ton G. van Leeuwen,<sup>c</sup> Klaas Nicolay,<sup>a,†</sup> and Gustav J. Strijkers<sup>c</sup>

<sup>a</sup>Eindhoven University of Technology, Biomedical Engineering, Biomedical NMR, Eindhoven, The Netherlands

<sup>b</sup>Swiss Federal Institute of Technology Zürich, Institute for Biomedical Engineering, Zürich, Switzerland

<sup>c</sup>Academic Medical Center, Biomedical Engineering and Physics, Amsterdam, The Netherlands

**Abstract.** A noninvasive method is introduced for quantification and visualization of fluence rate in light-irradiated biological tissues. The method is based on magnetic resonance thermometry (MRT) measurements of tissue temperature changes resulting from absorption of light. From the spatial-temporal temperature data, the generated heat is calculated. Finally, fluence rate maps are reconstructed by dividing the heat data by the tissue absorption coefficient. Simulations were performed using virtual MRT datasets based on analytically described fluence rate distributions, which could be accurately reconstructed by the method. Next, the approach was tested in gel phantoms. Resulting fluence rate maps matched well with theoretical predictions in a non-scattering phantom ( $R^2 = 0.93$ ). Experimental validation was further obtained in a scattering phantom, by comparing fluence rates to invasive fluence rate probe measurements along and perpendicular to the optical axis ( $R^2 \geq 0.71$  for both cases). Finally, our technique was applied *in vivo* in a mouse tumor model. The resulting fluence rates matched invasive probe measurements (Pearson's  $\rho = 0.90$ ,  $p = 0.0026$ ). The method may be applied to investigate the relation between light dose and biological response in light-based treatments, such as photodynamic therapy. It may also be useful for experimental validation of light transport models. © 2017 Society of Photo-Optical Instrumentation Engineers (SPIE) [DOI: 10.1117/1.JBO.22.3.036001]

**Keywords:** fluence rate; magnetic resonance imaging; thermometry; photodynamic therapy; laser-induced hyperthermia; mouse tumor model.

Paper 160809R received Nov. 28, 2016; accepted for publication Feb. 10, 2017; published online Mar. 1, 2017.

## 1 Introduction

In the fields of biomedical optics, light-based therapies, and optical diagnostics, the fluence rate  $\Phi$  is a key parameter, as it quantifies the local intensity of light. The (radiant energy) fluence rate  $\Phi$  ( $\text{W}/\text{m}^2$ ) at a given point in space is defined as “the radiant energy flux incident on a small sphere, divided by the cross-sectional area of that sphere.”<sup>1</sup> The local fluence rate determines the rate of absorption of optical energy per unit volume through  $Q(r) = \mu_a \Phi(r)$ , where  $Q$  is the absorbed power density ( $\text{W}/\text{m}^3$ ) and  $\mu_a$  the absorption coefficient ( $\text{cm}^{-1}$ ). Fluence rate is wavelength-dependent and integration of fluence rate over time gives the (radiant energy) fluence ( $\text{J}/\text{m}^2$ ).

In photodynamic therapy (PDT), the fluence rate plays an important role.<sup>2,3</sup> PDT is a cancer treatment that relies on a light-activated drug called photosensitizer (PS). Upon light absorption by this drug, highly reactive oxygen species are generated, which induce cell death. The therapeutic dose–response relation in PDT is far from completely understood, but it is known to depend on many parameters.<sup>4</sup> These parameters include the PS concentration in the tissue, the availability of tissue oxygen, and importantly, both the total fluence and the fluence rate. It is argued that at high fluence rates, excessive singlet

oxygen generation can lead to oxygen depletion, resulting in lower treatment effectiveness.<sup>5</sup> Therefore, the total fluence alone is not enough to characterize the PDT dose, but the spatial distribution of the fluence rate is needed.

If the irradiation conditions and the optical properties of the tissue of interest are known, the fluence rate can be calculated. Although analytical models of light transport exist,<sup>6</sup> these so-called radiative transfer equations (RTE) are usually difficult to solve. Therefore, a common approach is to use a diffusion model to approximate the RTE, which is easier to solve but can provide reasonably accurate fluence rate results. Alternatively, fluence rates can be obtained from Monte Carlo simulations of large numbers of individual photon trajectories.<sup>7</sup> This latter method requires heavy computations. Unfortunately, both methods require knowledge of tissue optical properties, such as absorption and scattering coefficients, which are often not available.

An alternative is to measure fluence rate directly using an invasive interstitial probe. Isotropic fluence rate probes are available with a small spherical tip of typically a few hundreds of micrometers in diameter made of a scattering material, which uniformly collect light from all incident angles.<sup>8</sup> The tip is mounted onto the end of a bare fiber, the other end of which is connected to a photodiode. When carefully calibrated, a fluence rate measurement with such a probe works well with an accuracy of 5% to 10%.<sup>9</sup> However, the method is highly invasive as the probe has to be pierced into the tissue, and small hemorrhages around the tip can disturb the measurement. Moreover,

\*Address all correspondence to: Tom J. L. Schreurs, E-mail: [t.j.l.schreurs@tue.nl](mailto:t.j.l.schreurs@tue.nl)

<sup>†</sup>This work was dedicated to Professor Klaas Nicolay, our friend, mentor, and a devoted researcher, who died on January 10, 2017. We will remember him for his great contribution to science and education in the field of biomedical NMR and his warm and inspiring personality.

such a probe provides only single-point information, whereas for proper evaluation of PDT, 3-D spatial information is needed.

To our knowledge, until now a noninvasive method to measure fluence rate in 2-D or 3-D in living tissue did not exist. We propose the use of *in vivo* magnetic resonance thermometry (MRT) for noninvasive estimation of fluence rate in tissues irradiated with visible or near-infrared light. Our method uses MRT temperature data to calculate the spatial-temporal heat source distribution that is induced by significant absorption of photons. The fluence rate distribution is subsequently derived by dividing the heat source term by the absorption coefficient of the tissue. The method was tested in gel phantoms and in mouse tumors. Results were in close agreement with invasive optical probe measurements. We expect that this method will lead to new insights with regard to photon transport in biological tissues and light dosimetry, e.g., for PDT.

## 2 Materials and Methods

### 2.1 Theory

The light-induced rate of heat energy  $Q$  (W/m<sup>3</sup>) generated in a tissue or material with absorption coefficient  $\mu_a$  equals  $Q = \mu_a \Phi$ , where  $\Phi$  is the fluence rate. Temperature change caused by such a heat source is described by the heat diffusion equation:

$$\rho c \frac{dT}{dt} = Q + k \nabla^2 T,$$

where  $\rho$  is the tissue or material density (kg/m<sup>3</sup>),  $c$  is the specific heat capacity [J/(kg \* K)], and  $k$  is the thermal conductivity [W/(m \* K)].<sup>10</sup> Throughout this study, we assumed that heat losses at tissue-air boundaries during the short time-course of the experiments were negligible. Moreover, we neglected convective heat transfer effects of blood perfusion. For biological tissues and water-based materials, temperature changes can be measured in 2-D or 3-D and as a function of time using MRT, as explained further on. If the discrete temperature data have a sufficient signal-to-noise ratio, the time derivative  $dT/dt$  and the Laplacian  $\nabla^2 T$  can be robustly calculated. The generated heat power density  $Q$  can then be calculated by filling in the heat equation, assuming the material properties  $\rho$ ,  $k$ , and  $c$  are known. The material properties for biological tissues are usually quite close to those of water, which are  $\rho = 1000$  kg/m<sup>3</sup>,  $k = 0.6$  W/(m \* K), and  $c = 4178$  J/(kg \* K). These values were used throughout the study, for both phantom and *in vivo* experiments. Values for specific tissue types are available in literature.<sup>11,12</sup> The fluence rate readily follows from the heat power density  $Q$  if the absorption coefficient is known, using  $\Phi = Q/\mu_a$ .

Calculation of the time derivative  $dT/dt$ , and especially, the second derivative  $\nabla^2 T$  is challenging, due to the noise in the MRT data. The derivatives  $dT/dt$  and  $\nabla^2 T$  were obtained separately by calculating the analytical derivative of local polynomial fits, performed at each pixel and each time point. To reduce computation time, the derivatives were calculated only within a spatial mask, defined by applying a threshold to the magnitude images of the thermometry data. For the time derivative at time point  $t_i$ , a second order polynomial fit was performed to a window of  $N$  time points around  $t_i$ . For simulations and *in vivo* experiments,  $N = 15$  was used, while  $N = 11$  was used for phantom experiments. The time curves were split in three

periods: before, during, and after laser irradiation. At the transitions between the periods, only the available time points from within that period were used for calculating the fits, because the curves are nondifferentiable at the transition. The polynomial fit functions and their analytical derivatives were evaluated at each time point, to obtain smoothed temperature curves and temperature derivative curves. The root mean squared error (RMSE) of the smoothed versus the original temperature curves was calculated, and a threshold was applied to the RMSE to exclude pixels with a low fit quality from the mask. Next, 3-D polynomials of the form  $T = a_0 + a_1x + a_2y + a_3z + a_4xy + a_5xz + a_6yz + a_7x^2 + a_8y^2 + a_9z^2$  were fitted to the smoothed temperature data within a spherical neighborhood of radius  $R$  around each pixel. For simulations and *in vivo* experiments,  $R = 3.75$  mm was used, while  $R = 3.0$  mm was used for phantom experiments. To improve the signal-to-noise ratio and fit quality, pixels outside the mask were excluded from the neighborhood. The Laplacian at each point was obtained by calculating  $\nabla^2 T = 2(a_7 + a_8 + a_9)$ .

### 2.2 Simulations

The feasibility of our method was tested on a 3-D virtual temperature dataset, obtained by simulating the heat generation and transport by a predefined fluence rate distribution in a nonscattering phantom with known thermal properties and absorption coefficient  $\mu_a$ . A point light source, centered in a  $30 \times 30 \times 30$  mm<sup>3</sup> volume of interest, was defined on a tetrahedral mesh of 80,412 points. Between  $t = 120$  and  $t = 420$  s of the simulation, the light source was switched on with a fluence rate distribution of  $\Phi(r) = A \exp(-\mu_a r)/r$ , with amplitude  $A = 12.5$  W/m and  $r$  the radial distance from the point source. In an infinite homogeneous medium with absorption coefficient  $\mu_a = 0.5$  cm<sup>-1</sup>, such a light source produces heat with a power density of  $Q(r, t) = \mu_a \Phi(r)$  for  $120 \leq t \leq 420$ , and  $Q(r) = 0$  otherwise. The heat transfer equation ( $\rho c \frac{dT}{dt} = k \nabla^2 T + Q$ ) was solved using finite-element method functions in the partial differential equation (PDE) toolbox of MATLAB R2016a. Temperature maps were generated from  $t = 0$  to 1020 s in steps of 10 s. In five slices, centered at  $z = -2.2, -1.1, 0, 1.1$ , and  $2.2$  mm around the point source, the temperature maps were interpolated to a Cartesian grid of  $64 \times 64$  pixels, resulting in 0.47-mm spatial resolution, similar to our *in vivo* measurements. A second temperature dataset was obtained by adding Gaussian noise with a standard deviation of 0.43°C, to assess the effect of noise on the fluence rate calculations. Subsequently, the fluence rate calculation was performed on the noiseless and noisy temperature datasets, and the result was compared to the input fluence rate.

### 2.3 Fluence Rate Probe

A model IP85 isotropic light probe (Medlight, Ecublens, Switzerland) was used for validation of fluence rate estimations in phantom and *in vivo* experiments. The probe consists of a ceramic spherical bulb mounted onto the distal end of a bare optic fiber. A fraction of the light collected by the bulb was guided through the fiber and detected by a photodiode on the proximal fiber end. The bulb collected light from all incident angles with nearly identical efficiency, except for the blind spot created by the fiber. The overall efficiency of the probe was calibrated, by placing the fiber in a light beam with known irradiance. Since the efficiency of the probe depends

on the refractive index of its ambient medium,<sup>13</sup> the calibration was done in water, which has a similar refractive index as tissue. The light was produced by a fiber-connected 655-nm laser (model WSLB-650-002-H, WaveSpectrum, Beijing, China). The fiber output was placed in front of an optical diffuser, to generate a 20-deg diverging beam with uniform light intensity profile. The irradiance of the beam was first quantified using a photodiode (model S121C, Thorlabs, Newton, New Jersey). Next, the photodiode was removed and the beam was aimed orthogonally onto the surface of a degassed water bath. The fiber was placed horizontally just below the water surface, with the bulb in the center of the beam, at the same longitudinal distance as the photodiode. The water container was made of black plastic, to minimize light reflections. The assumed irradiance at the probe was corrected for 2% reflectivity at the air–water surface. Since the probe was only slightly below the water surface and the divergence of the beam was small, no correction was applied for the change in beam diameter due to refraction. The optical power at the proximal end of the probe fiber was measured with a photodiode (model S150C, Thorlabs). A calibration factor was obtained by dividing the irradiance at the probe by the measured fiber power output.

## 2.4 Phantom Preparation

Gel phantoms were prepared by adding 4% w/v gelatin from porcine skin (G2500, Sigma Aldrich, St. Louis, Missouri) to ultrapure water at 30°C while continuously stirring. Desired amounts of Evans Blue (E2129, Sigma Aldrich) and anatase titanium dioxide (232033, Sigma Aldrich) were added, as absorbing and scattering agents, respectively. Next, 0.1% v/v formaldehyde (252549, Sigma Aldrich) was added to facilitate cross-linking and the solution was heated to 45°C. It was then poured into the desired container or mold, which was placed in a vacuum chamber at 150 mbar for 15 min to remove air bubbles. The samples were stored in a 4°C refrigerator to fully crosslink overnight and used the next day.

## 2.5 Phantom Characterization

The absorption coefficient as a function of Evans Blue concentration in the gelatin samples was determined by transmission spectroscopy. Samples were prepared *in duplo*, as described above in cuvettes (7590-05, Brand, Wertheim, Germany) with a path length of  $d = 10$  mm. Evans Blue concentrations of 2.53, 5.05, 10.1, 20.3, and 40.5 mg/L were prepared, and no  $\text{TiO}_2$  was added. Two reference samples were prepared in the same way, but without Evans Blue. In a dark room, the cuvettes were placed in a cuvette holder (Ocean Optics, Dunedin, Florida), in between opposing ends of two optical fibers. One fiber was connected to a white light source (DH2000, Ocean Optics), while the other one was connected to a spectrophotometer (AvaSpec-ULS2048, Avantes, Apeldoorn, The Netherlands). Transmittance  $T$  at 655 nm was calculated by dividing the signal intensities of each sample by that of a reference sample, after subtracting a dark measurement signal from both sample signals. The absorption coefficient in  $\text{cm}^{-1}$  was then calculated as  $\mu_a = -\ln T/d$ .

## 2.6 Phantom Magnetic Resonance Experiments

MRI experiments were performed with a 7 T scanner (BioSpec 70/30 USR, Bruker) using a quadrature 72-mm-diameter

transmit and receive birdcage coil.  $T_2$ -weighted anatomical reference images were acquired using a multislice spin echo scan, with five axial slices centered on the light spot. Scan parameters were as follows: repetition time (TR) = 1000 ms, echo time (TE) = 30 ms, matrix =  $128 \times 128$ , slice thickness = 1.0 mm, slice gap = 0.1 mm, field of view (FoV) =  $6 \times 6$  cm<sup>2</sup>. The same geometry was used for all scans.  $T_1$  and  $T_2$  values of the phantom were determined with RARE relaxometry acquisitions, with the following parameters: RARE factor = 2, TE = 11, 33, 55, 77, 99 ms, TR = 593, 813, 1096, 1491, 2155, 5000 ms.  $T_2^*$  values were determined with a multigradient echo sequence, with the following parameters: TE<sub>min</sub> = 2.9 ms,  $\Delta\text{TE} = 3.5$  ms, TE<sub>max</sub> = 60.4 ms, flip angle (FA) = 30 deg, TR = 1500 ms. For MRT, a FLASH sequence was used with TE approximately equal to  $T_2^*$  (typically between 7 and 10 ms) and FA equal to the Ernst angle (typically between 12 and 14 deg). Other scan parameters were TR = 76 ms and scan time = 9.7 s. After acquisition of five baseline scans, the thermometry acquisition was repeated for the duration of the heating experiments.

A custom-built setup was used to perform laser-induced heating of the phantom inside the MRI scanner. The light from a 655-nm laser (model WSLB-650-002-H, WaveSpectrum, Beijing, China) was guided into the magnet by an optical fiber, collimated to an approximately parallel beam, and reflected downward by a prism onto the phantom. The diameter of the projected spot could be adjusted by changing the distance between fiber and collimator lens, and was between 0.65 and 0.90 cm in all experiments. Before each experiment, power output of the collimated beam was measured with an optical power meter. The spot size of the light bundle was measured with a ruler, and the laser current was adjusted to achieve the desired irradiance, assuming a uniform beam profile. Irradiance settings of 400 and 576 mW/cm<sup>2</sup> were used. During the heating experiments, the laser controller (model ITC4005, Thorlabs) was switched on after 1 min and off after 11 min, and was triggered by the MR pulse sequence. The complete experiment duration was 31 min, acquiring thermometry maps during a 20-min cooling period as well.

$B_0$  magnetic field drift correction was performed based on a linear space dependent phase correction map from the MR signal phase images, similar to De Poorter et al.<sup>14</sup> Four horizontally positioned cuvettes filled with mineral oil were positioned around the gel sample in the corners of the imaging FoV. The phase correction map was obtained by a least squares fit plane through the phase of the four reference phantoms. The phase in the phantom was corrected at each time point by subtracting the phase correction map. Temperature maps were obtained by calculating the phase difference images  $\Delta\phi$  with respect to the average of the five baseline scans ( $\phi_0$ ), and division by the PRF change coefficient  $\alpha = 0.01$  ppm/°C, the gyromagnetic ratio  $\gamma$ , the echo time TE, and the magnetic field strength  $B_0$ , according to  $\Delta T = \Delta\phi/(\alpha\gamma B_0 \text{TE})$ .

## 2.7 Phantom Validation

For validation of MRT-based fluence rate results, fluence rate probe measurements were performed in similar phantoms as used in the MR experiments. The same optical setup was used to produce similar beam geometry. For quantification of the fluence rate along lines perpendicular to the optical axis of the light beam, the probe was inserted 2 cm into the side of the phantom, while the beam was projected onto the top



surface. Using a motorized linear stage, the optical setup was then moved over the phantom in steps of 0.5 mm, such that the beam center traveled a straight path right above the probe tip. The depth  $z$  of the probe with respect to the phantom's top surface was measured with a caliper after slicing the phantom near the probe tip. The experiment was repeated in multiple phantoms, each time with the probe at a different depth. For measurement of the fluence rate profile along the optical axis, the probe was inserted into the bottom of the phantom, while the beam was again aimed onto the top surface and centered above the probe. The probe was inserted further into the phantom, in steps of 0.5 mm, until the tip emerged from the top surface.

## 2.8 Mouse Cancer Model

All animal experiments were approved by the Animal Care and Use Committee of Maastricht University (protocols: 2012-139 and 2014-011). The maintenance and care of the experimental animals were in compliance with the guidelines set by the institutional animal care committee, accredited by the National Department of Health.

CT26.WT murine colon carcinoma cells (American Type Culture Collection (ATCC), CRL-2638) were cultured at 5% CO<sub>2</sub> and 37°C in RPMI-1640 medium (Invitrogen, Breda, The Netherlands), supplemented with 50 U/ml penicillin/streptomycin (Lonza Bioscience, Basel, Switzerland) and 10% fetal bovine serum (Greiner Bio-One, Alphen a/d Rijn, The Netherlands). Early passages (9-13) of the original ATCC batch were used for inoculation and  $2 \times 10^6$  cells were inoculated subcutaneously in the right hind limb of 10- to 12-week-old BALB/c mice (Charles River, Maastricht, The Netherlands). Tumors became palpable at 3 to 5 days after inoculation. Experiments were performed when tumor volumes were between 271 and 621 mm<sup>3</sup>, approximately after 10 days. During MR imaging, mice were anesthetized using isoflurane (3.5% for induction, 1% to 2% for maintenance) in medical air flowing at 0.4 L/min. Breathing rate was monitored with a pressure balloon. Body temperature was monitored using a rectal probe, and kept at 36°C to 37°C using a warm water circuit. In the course of the study,  $n = 9$  mice were used, of which some were scanned two times on different days.

## 2.9 In Vivo Experiments

The tumor-bearing hind limb was shaved before the experiment. A 19G needle was used to make a small perforation in the skin to facilitate insertion of a probe. Mice were placed in the same setup as used for phantom experiments. The hind limb was gently fixed in a stretched position, with the tumor on top and as close as possible to the isocenter of the MR scanner. An isotropic fluence rate probe was inserted in the tumor through the skin perforation. The penetration depth of the probe was deduced from the position of a pen marking on the fiber. Similar to the phantom experiments, a beam of 655-nm light was projected downward onto the tumor. The center of the laser beam was positioned in the same axial slice as the probe. Irradiances of 300, 400, and 500 mW/cm<sup>2</sup> were applied for 5 min, and the beam diameter was between 0.65 and 0.90 cm. The central MR slice was longitudinally aligned with the tip of the probe. An absorption coefficient of  $\mu_a = 1.0 \text{ cm}^{-1}$  was assumed for the fluence rate calculation, which is within the range of values for tumors reported in literature.<sup>12,15</sup>

In order to demonstrate the MRT technique, a custom fiber optic temperature probe (Neoptix, Quebec, Canada) embedded in a 1-mm-diameter carbon needle was inserted into the tumor of one mouse, instead of a fluence rate probe. For this animal, the duration of laser heating was 13 min at an irradiance of 0.71 W/cm<sup>2</sup> and a beam diameter of 0.8 cm.

## 3 Results

### 3.1 Magnetic Resonance Thermometry Demonstration

Within the MRI research field, MRT is an established technique, although there are only a few demonstrations of MRT in small animals at 7 T.<sup>16</sup> To assess accuracy and precision of the MRT, the MRI-based temperature data were compared to measurements with the tumor interstitial temperature probe (Fig. 1). The standard deviation of the temperature in a tumor region of interest (RoI) in a preheating temperature map was 0.43°C. Since MRT is a subtraction-based method, only temperature changes can be measured, relative to the starting temperature. Therefore, the robustness of the measurements decreases with the duration of the experiment, despite the use of field drift correction. For example, in Fig. 1(c), the RMSE of MRT versus the temperature probe increases from 0.49, to 0.90, and 1.29°C in the 1st, 15th, and 30th min, respectively. The temperature stability of *in vivo* experiments without heating was assessed by calculating the average absolute temperature drift in the final (20th) minute in a tumor RoI. The mean and standard deviation of this temperature stability over all *in vivo* experiments included in this study ( $n = 10$ ) was  $1.20 \pm 0.76^\circ\text{C}$ .

### 3.2 Simulations

To demonstrate the feasibility of MRT-based fluence rate calculation, 3-D simulations were first performed using virtual thermometry datasets, calculated for a known predefined fluence rate. Figure 2(a) provides a schematic outline of the simulation, with snapshot images of the central slices of the fluence rate distribution, temperature maps, the virtual MRT maps, and the final fluence rate map. The maximum temperature elevation at the center was 5.7°C. For the noiseless case, the spatial RMSE of the resulting fluence rate was only 8.8 mW/cm<sup>2</sup> for pixels located farther than 1.5 mm from the point source and calculated over the entire FoV, whereas the predefined fluence rate was larger than 100 mW/cm<sup>2</sup> for all pixels at a distance within 8.3 mm from the point source. The largest spatial RMSE was found close to the light source center, where the fluence rate asymptotically approaches infinity. Even with added Gaussian noise with a standard deviation similar to a typical *in vivo* MRT measurement ( $\sigma_T = 0.43^\circ\text{C}$ ), the fluence rate could be estimated with acceptable confidence (spatial RMSE = 66.2 mW/cm<sup>2</sup>). In Fig. 2(b), the time curve of the fluence rate in a pixel close to the virtual light source is shown (top), as well as a spatial profile along the radial axis of the light source (bottom). For the time curves, the temporal RMSE of the estimated versus the actual fluence rate was 21.8 and 60.6 mW/cm<sup>2</sup>, for the simulation without and with added noise, respectively. For the spatial profile, the spatial RMSE's were 24.4 and 36.7 mW/cm<sup>2</sup>, for the noiseless case and the added-noise case, respectively.

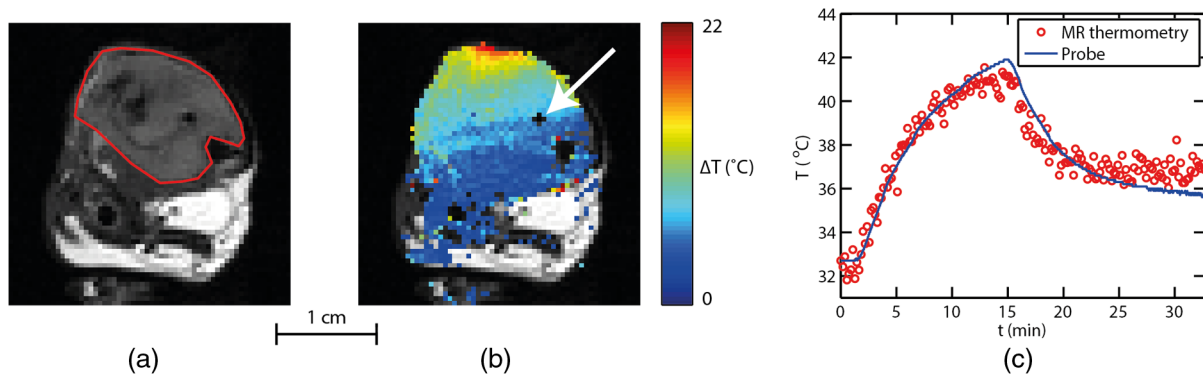


**Fig. 1** Demonstration of the MRT technique. (a) Anatomical reference image of the axial cross-section of a mouse hind limb. The red contour indicates the outline of the tumor. (b) Example of a temperature map at  $t = 14$  min, showing the temperature increase after 13 min of laser-induced heating. The temperature map shows a strong increase in the top of the tumor, where the light entered the tissue. The white arrow indicates the position of the temperature probe. (c) In a pixel next to the probe, the MRT data followed the probe temperature with an RMSE of  $0.74^{\circ}\text{C}$ , calculated over the entire duration of the experiment. The temperature starting point of the MRT data was set equal to the first measurement value of the probe.

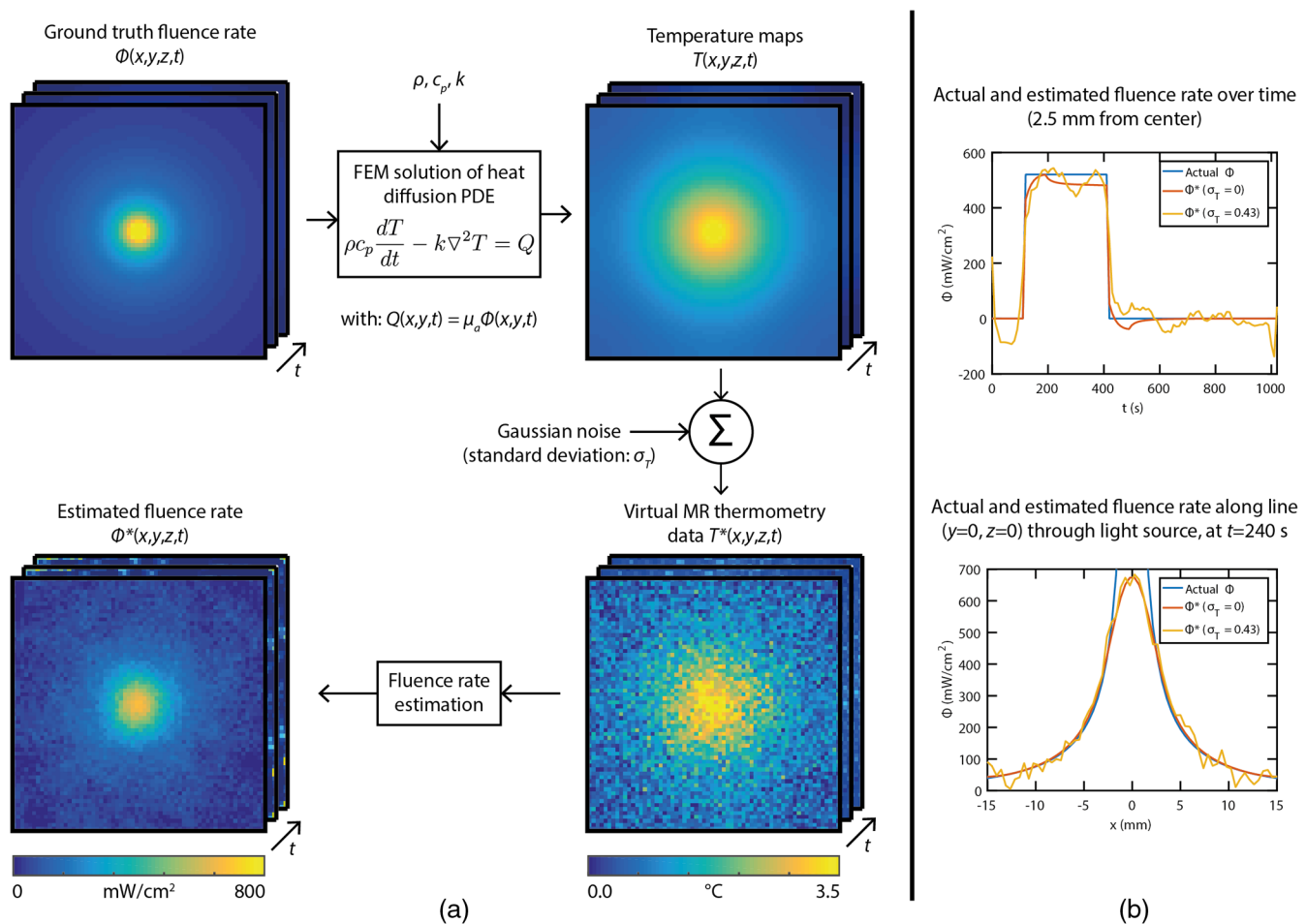


**Fig. 2** (a) Flow chart of simulation and example data showing the feasibility of the fluence rate calculation. A finite element method was used to solve the heat diffusion partial differential equation, to generate a spatial-temporal dataset of the temperature increase induced by an analytically described light source. The temperature dataset was solved on a fine tetrahedral mesh and then resampled to a Cartesian grid. By adding Gaussian noise ( $\sigma = 0.43$ ) to this dataset, a virtual MRT dataset was obtained. Fluence rate calculation was performed on this dataset, resulting in an estimated light-source map. The example shows a good resemblance with the ground truth fluence rate, even with added Gaussian noise. (b) In the top figure, the ground truth and estimated fluence rate in a single pixel are shown as a function of time, based on MRT data with and without added noise. In the bottom, the fluence rate profiles along a line through the point source are shown.

### 3.3 Phantom Experiments

To calculate the dependence of the absorption coefficient  $\mu_a$  on the Evans Blue concentration in 4% gelatin phantoms, a transmission spectroscopy experiment was performed. The absorption coefficient at 655-nm wavelength increased linearly with the concentration of Evans Blue (Pearson's  $\rho = 0.9998$ ). A linear fit through all data points led to the following equation:  $\mu_a = 94.2[\text{EB}] + 0.07 \text{ cm}^{-1}$ , with [EB] the concentration of Evans Blue in g/L.

Next, the fluence rate estimation method was tested in a non-scattering gelatin phantom, which was heated by a laser beam while temperature changes were measured by MRT. The result is displayed in Fig. 3, displaying the calculation steps from temperature map to a fluence rate map. The temperature strongly increased where the light entered the phantom, but over time the rate of increase declined [Figs. 3(a) and 3(e)]. When the laser was switched on, the time derivative was positive and gradually approaching zero [Figs. 3(b) and 3(f)]. After switching off the laser, the time derivative became negative as the sample cooled down again. The Laplacian [Figs. 3(c) and 3(g)] was negative in most of the irradiated region during illumination but quickly went back to zero after the laser was turned off. The calculated fluence rate map [Fig. 3(d)] displayed a positive band along the beam axis, with decreasing values as function of penetration depth. The calculated fluence rate in a pixel near the probe [Fig. 3(h)] was close to the probe value during laser irradiation and returned to practically zero afterward. The median fluence rate in this pixel was  $266 \text{ mW/cm}^2$ , which was an underestimation of 27% compared to the median probe value of  $363 \text{ mW/cm}^2$ .

Further validation of the MRT-based fluence rate estimation was performed in a nonscattering gelatin phantom ( $20.3 \text{ mg/L}$  Evans Blue,  $\mu_a = 1.98 \text{ cm}^{-1}$ ) and a turbid gelatin phantom ( $5.04 \text{ mg/L}$  Evans Blue and  $2.50 \text{ g/L}$   $\text{TiO}_2$ ,  $\mu_a = 0.544 \text{ cm}^{-1}$ ). Both phantoms were irradiated for 5 min with a 0.8-cm wide collimated beam, normally incident onto the top surface. Figure 4(a) shows the fluence rate map for the nonscattering phantom. In Fig. 4(b), the fluence rate as a function of penetration depth  $z$  along the beam axis was compared to the theoretically expected profile based on Beer–Lambert's law:  $\Phi(z) = \Phi_0 \exp(-\mu_a z)$ .  $\Phi_0$  is the fluence rate value in the top layer ( $z = 0$ ) of the phantom, and was obtained by reducing the irradiance ( $E = 400 \text{ mW/cm}^2$ ) by the specular reflection loss, expressed by the reflectance  $R_{\text{sp}} = [(n_0 - n_1)/(n_0 + n_1)]^2$ , where  $n_0$  and  $n_1$  are the refractive indices of air and the gelatin mixture, respectively. Assuming that  $n_0 = 1.0$  and  $n_1 = 1.33$ , 98% of the irradiance was expected to be transmitted into the phantom, so  $\Phi_0 = 392 \text{ mW/cm}^2$ . Based on the Evans Blue concentration of the phantom, the expected absorption coefficient was  $\mu_a = 1.98 \text{ cm}^{-1}$ . The RMSE of the experimental versus the theoretical fluence rate along the beam axis was  $23.6 \text{ mW/cm}^2$  (6.0% compared to  $\Phi_0$ ), and  $R^2$  was 0.929. The experimental fluence rate generally was a bit lower than theoretically predicted, especially in the top layer of the phantom.

The fluence rate map of the scattering phantom [Fig. 4(c)] shows a shallower light penetration than for the nonscattering phantom. The fluence rate in the top layer exceeded the applied irradiance values. Figures 4(d) and 4(e) show comparisons between the MRT-based fluence rate and probe measurements along the beam axis and along radial lines at four different

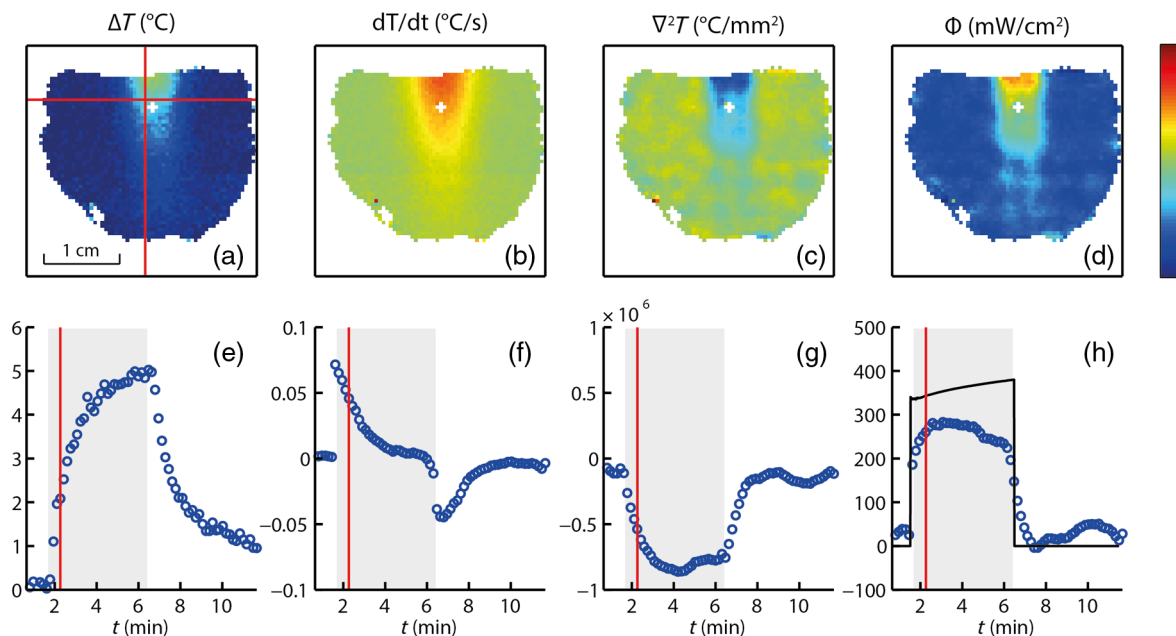


**Fig. 3** Demonstration of the fluence rate calculation in a gelatin phantom with Evans Blue and no scattering material. The top row contains maps of (a) the temperature increase  $\Delta T$ , (b) its time derivative  $dT/dt$ , (c) the Laplacian  $\nabla^2 T$ , and (d) the resulting fluence rate  $\Phi$ , at a time point just after the laser was turned on. The bottom row (e–h) shows time curves of the same quantities, in the pixel indicated by the red crosshairs in the  $\Delta T$  map. The red line in the time plots indicates the time point to which the maps correspond. The color bar applies to all four maps, and the range of each map is the same as the vertical axis of the corresponding time curve. The gray box indicates the time interval during which the laser was turned on. The black curve in the fluence rate time plot shows the fluence rate measured by the probe. The gap in the maps reveals the location of the probe.

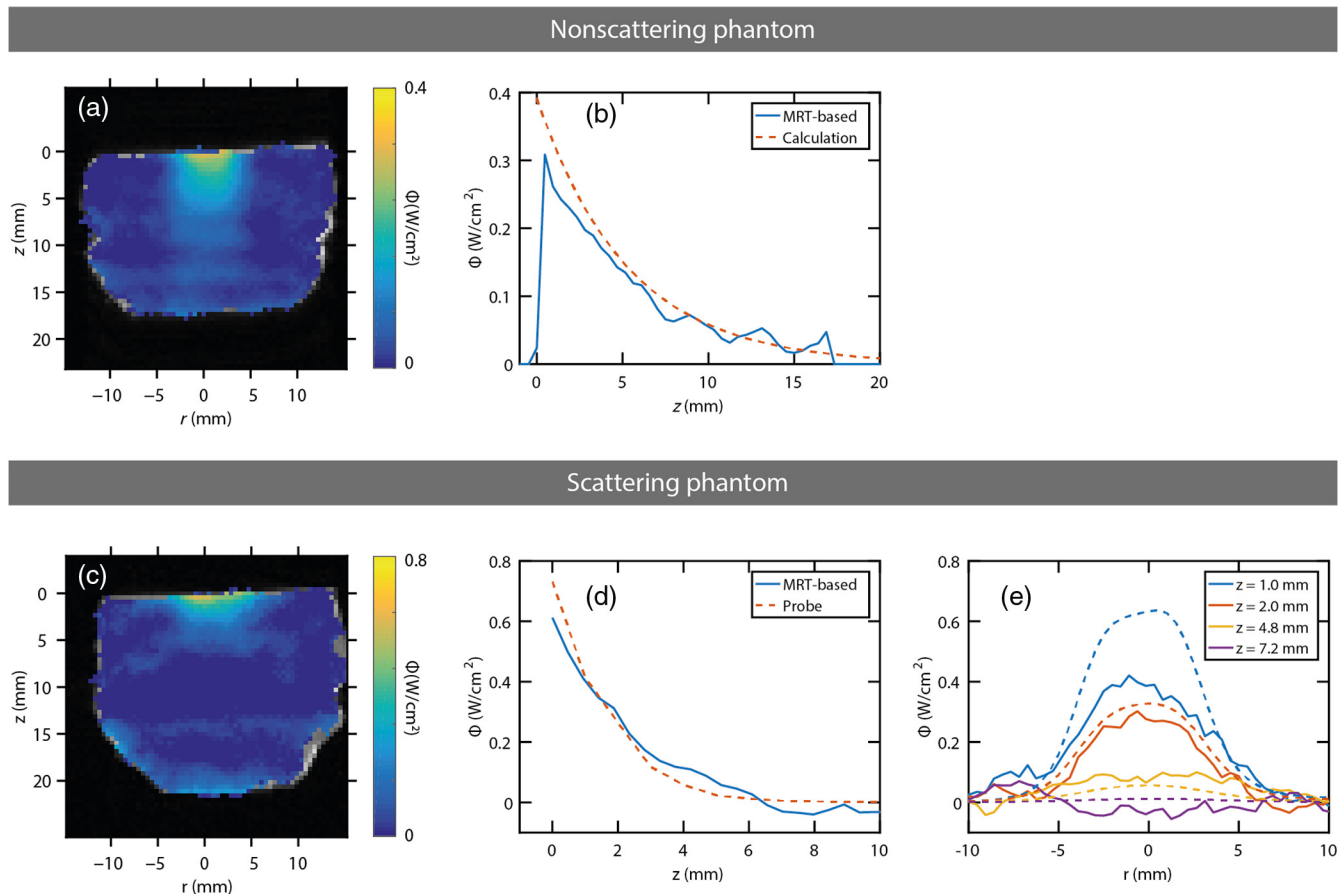


**Fig. 4** Validation of MRT-based fluence rate maps of two laser-irradiated phantoms. (a) Fluence rate map for a gelatin phantom with 20.3 mg/L Evans Blue and without a scattering material. (b) Comparison of the fluence rate attenuation along the optical axis (blue solid line) to the expected exponential decay profile (red dashed line). (c) Fluence rate map for a gelatin phantom containing 5.04 mg/L Evans Blue and 2.5 g/L  $\text{TiO}_2$ . (d) Comparison of the fluence rate attenuation along the optical axis (blue solid line) to probe measurements (red dashed line). (e) Comparison of the MRT-based fluence rate (solid lines) to probe measurements (dashed lines) along radial lines at four different depths  $z$  below the phantom surface. The two fluence rate maps show the median of the fluence rate over the interval during which the laser was turned on. Note that the color bars of both phantoms have different ranges.

depths. The spatial RMSE for the longitudinal profile was  $51.1 \text{ mW/cm}^2$  (7.0%), whereas for the radial profiles, it was 129.4 (17.7%), 34.5 (4.7%), 35.7 (4.9%), and 34.7 (4.7%)  $\text{mW/cm}^2$  at  $z = 1.0, 2.0, 4.8$ , and  $7.2 \text{ mm}$ , respectively. The percentages are all with respect to the maximum probe fluence rate along the optical axis.  $R^2$  values were 0.942 for the longitudinal profile, and 0.714 and 0.918 for the radial profiles  $z = 1.0$  and  $2.0 \text{ mm}$ . For the other two depths,  $R^2$  was not calculated, because the fluence rates were approximately zero.

### 3.4 In Vivo Experiments

Finally, the method was demonstrated *in vivo* in a mouse tumor model. An example of these experiments is shown in Fig. 5. Essentially, the observations were similar to those in the phantom experiment. The overall fluence rate distribution in the tumor was as expected: high values in the upper region, where the beam entered the tissue, but a more diffuse profile than for the nonscattering phantom. In most pixels, the fluence rate time curves were close to zero when the laser was off, and increased when it was on. In general, the temperature SNR of the *in vivo* experiments was lower than the phantom

experiments. Signal voids were observed in some tumors, especially when they were scanned for the second time, possibly due to hemorrhages induced by the probe or laser heating. In addition, some temperature drifts were observed after laser irradiation in regions of most tumors, e.g., slow increases after initial decrease or decrease below zero. One mouse was excluded from analysis, because the signal void around the probe was too large to reliably calculate  $\nabla^2 T$  in large parts of the tumor. The correlation between the fluence rate measured by the probe and the MRT-based fluence rate near the probe was statistically significant ( $p = 0.896$ ,  $p = 0.0026$ ), as shown in Fig. 6. The median value of the fluence rate over the interval during laser irradiation was used. A linear fit through the data points resulted in a slope somewhat below unity, which was caused mostly by the two data points with the largest probe values. All the other data points were closer to the identity line.

## 4 Discussion

A method was presented for quantification of fluence rate in laser-irradiated biological tissues, using MRT measurements. In this article, we provided a proof-of-concept and demonstrated the feasibility of the technique in simulations, phantom



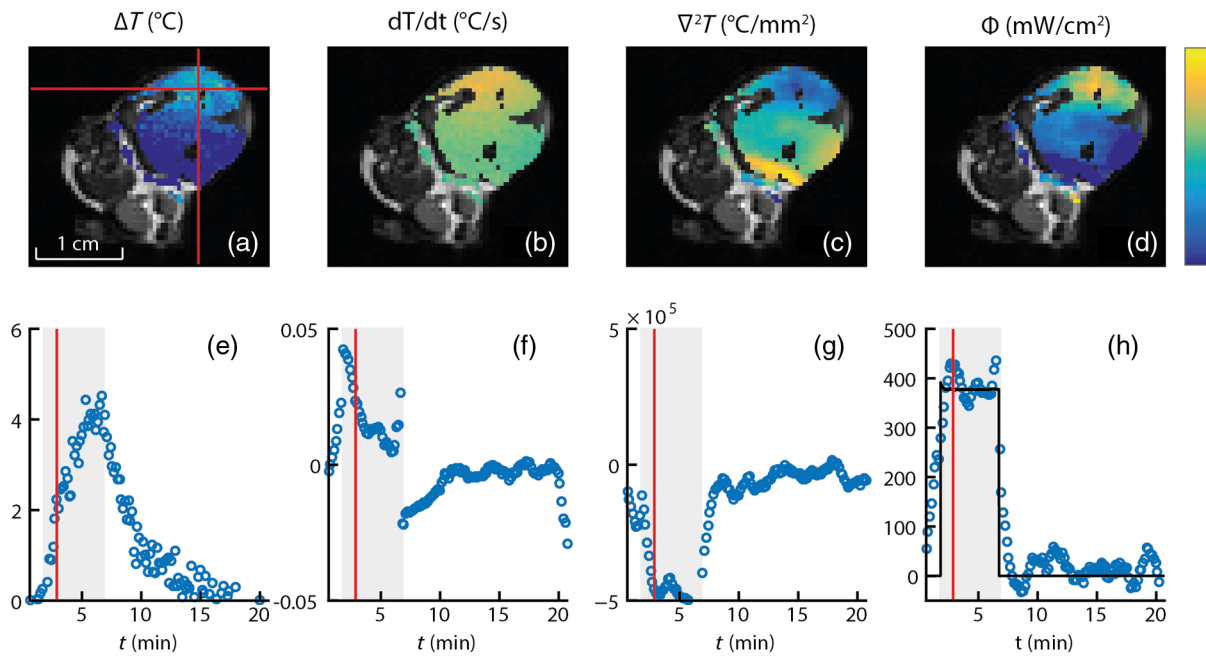


**Fig. 5** Example of *in vivo* fluence rate calculation. The top row shows maps of (a) the temperature increase  $\Delta T$ , (b) its time derivative  $dT/dt$ , (c) the Laplacian  $\nabla^2 T$ , and (d) the resulting fluence rate  $\Phi$ , at a time point just after the laser was turned on. The maps are presented as color overlays over a grayscale anatomical reference image. The bottom row (e–h) shows time curves of the same quantities, in the pixel indicated by the red crosshairs in the  $\Delta T$  map. The probe was located just below this pixel. The red line in the time plots indicates the time point to which the maps correspond. The colorbar applies to all four maps, and the range of each map is the same as the vertical axis of the corresponding time curve. The gray box indicates the time interval during which the laser was turned on. The black curve in the fluence rate time plot shows the fluence rate measured by the probe.

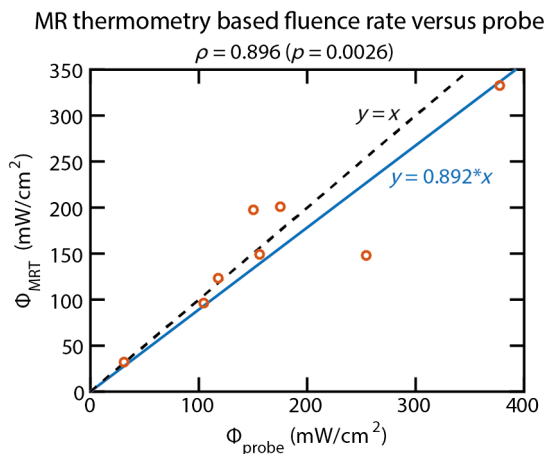


**Fig. 6** Scatter plot of the MRT-derived fluence rates of *in vivo* experiments, compared to the probe values. Each dot represents one experiment. The correlation coefficient is displayed above the figure and was statistically significant. The blue solid line is a linear fit through the origin. The identity line is displayed as a dashed black line.

experiments, and *in vivo* experiments. The method requires that the absorption coefficient of the tissue is known and that the tissue is heated up at least a few degrees by the light source. If these requirements are met, the method provides spatial–temporal visualization of fluence rate. Simulations demonstrated that the method provides results that accurately match with ground truth fluence rate data, depending on the SNR of the

MRT data. In the phantom experiments, it was shown that the calculated fluence rate profiles correspond well with theoretical predictions, and also with fluence rate probe measurements. Finally, the method proved to be feasible *in vivo* in a mouse solid tumor model, and a good correlation with fluence rate probe data was found. To our knowledge, no other noninvasive method exists for measurement of fluence rate.

The main anticipated application of our method is PDT-related research, e.g., to study the relation between light dose and therapeutic response. The method enables visualization of light penetration, which can be spatially compared to histologically determined tissue damage. However, the method might also be useful for general biomedical optics research, e.g., for experimental validation of models of light transport. Furthermore, it may be possible to estimate tissue optical properties from the fluence rate data, by fitting light transport models.

One drawback of the technique is that it requires knowledge of the absorption coefficient. The estimated fluence rate is inversely proportional to the absorption coefficient, so a relative error directly translates into a similar relative error in fluence rate. For example, the estimation that  $\mu_a = 1 \text{ cm}^{-1}$  for the *in vivo* experiments may have been too high, which could explain the underestimation of fluence rate compared to the probe measurements in Fig. 6. On the other hand, MRI provides excellent soft-tissue contrast, and therefore, offers the possibility to identify different tissue types. We suggest that anatomical MRI images, combined with a library of absorption coefficients for different types of tissues, can be used to create reasonably accurate maps of  $\mu_a$ , which can be used as input for our method.

Furthermore, it might be possible to extract the absorption coefficient from the heat source distribution. In the simple case of a broad uniform irradiation of a nonscattering material with homogeneous absorption coefficient,  $\mu_a$  can be estimated from the effective light penetration depth. For tissues with non-homogeneous  $\mu_a$ , a more sophisticated approach would be required. For example, one could think of an inverse Monte Carlo simulation, in which the spatial distribution of the absorption coefficient is searched iteratively. Once again, MRI information can be used to obtain anatomical information and classify tissue types, reducing the number of unknown absorption coefficients to the number of different tissue types, instead of the number of pixels.

In some of the *in vivo* experiments, conspicuous temperature drifts were observed toward the end of the measurement. Instead of returning to the initial tissue temperature, some regions showed negative temperature changes or temperature increases after initially cooling down when the laser was turned off. These apparent temperature effects may be artifacts, possibly related to hyperthermia-induced tissue changes. Tissue temperature increases can lead to changes in perfusion, hemorrhages, and tissue swelling<sup>17</sup> and lead to bias in the MRT results. This probably did not significantly affect our fluence rate results, since the heating period was short. However, fluence rate results of experiments with longer heating periods should be interpreted with care.

In the heat diffusion model that was used in this study, blood perfusion effects were neglected. It is known that blood vessels can act as heat sinks.<sup>10</sup> The tumor model that we used is well perfused but contains only capillaries, much smaller than the MRI resolution. Therefore, we expect that the cooling effect of heat convection through blood flow was insignificant in our experiments. However, the importance of perfusion on the fluence rate calculation should be investigated in future work. Excellent MRI methods exist for quantification of blood perfusion,<sup>18</sup> which might be useful to correct for the cooling effect of blood circulation.

Calculation of the Laplacian is the most challenging part of the method, especially for low SNR temperature data and at the edges of the phantom or tissue. For example, the accuracy along the radial profile just below the surface ( $z = 1$  mm) of the scattering phantom [Fig. 4(e)] was relatively low. The obtained estimates for the Laplacian depend on the neighborhood size used for the polynomial fit. We observed that a smaller neighborhood radius leads to better accuracy at the edges, at the price of higher overall variance in fluence rate results. Furthermore, better estimates for the Laplacian may be found using true 3-D data with full isotropic resolution. A 2-D multislice MR technique was used in the current study. The spatial resolution in the  $z$ -direction was therefore lower than in the other directions. Although 3-D MRI acquisitions with good resolution in all dimensions are possible, standard MRI techniques would result in unacceptably long scan times. Acceleration techniques for MRI are available to obtain high-resolution 3-D temperature data, without compromise with regard to temporal resolution.<sup>19</sup>

## 5 Conclusion

A noninvasive method for quantitative mapping of fluence rate in biological tissues was demonstrated, based on MRT. The feasibility of the method was established in simulations and phantom experiments. In the experiments, the resulting fluence rates matched excellently with theoretically predicted values, and the

spatial profiles also corresponded well with invasive probe validation measurements. Finally, the method was tested in a mouse tumor model, showing its *in vivo* potential. The method can be useful for assessing the dose–response relation in PDT studies but may also be applicable for fundamental biomedical optics research.

## Disclosures

The authors declare that they have no relevant financial interests in the manuscript and that no other potential conflicts of interest exist.

## Acknowledgments

This work is supported by NanoNextNL, a micro and nanotechnology consortium of the Government of the Netherlands and 130 partners.

## References

1. ISO 31/6, *Quantities and Units of Light and Related Electromagnetic Radiations*, 2nd ed., International Organization for Standardization, Switzerland (1980).
2. T. J. Dougherty et al., "Photoradiation therapy II - cure of animal tumors with hematoporphyrin and light," *J. Natl. Cancer Inst.* **55**(1), 115–121 (1975).
3. P. Agostinis et al., "Photodynamic therapy of cancer: an update," *CA: Cancer J. Clin.* **61**, 250–281 (2011).
4. I. J. Macdonald and T. J. Dougherty, "Basic principles of photodynamic therapy," *J. Porphyrins Phthalocyanines* **5**(02), 105–129 (2001).
5. T. M. Sittnik, J. A. Hampton, and B. W. Henderson, "Reduction of tumour oxygenation during and after photodynamic therapy in vivo: effects of fluence rate," *Br. J. Cancer* **77**(9), 1386–1394 (1998).
6. S. Chandrasekhar, *Radiative Transfer*, Dover, New York (1960).
7. L. V. Wang, S. L. Jacques, and L. Zheng, "MCML—Monte Carlo modeling of light transport in multi-layered tissues," *Comput. Methods Programs Biomed.* **47**(1995), 131–146 (1995).
8. W. L. Star, "Light dosimetry for photodynamic therapy by whole bladder irradiation," *Photochem. Photobiol.* **46**(5), 619–624 (1987).
9. J. P. Marijnissen and W. M. Star, "Performance of isotropic light dosimetry probes based on scattering bulbs in turbid media," *Phys. Med. Biol.* **47**(1), 2049–2058 (2002).
10. A. J. Welch and M. J. C. van Gemert, Eds, *Optical-Thermal Response of Laser-Irradiated Tissue*, 2nd ed., Springer, Dordrecht, The Netherlands (2011).
11. R. L. McIntosh and V. Anderson, "A comprehensive tissue properties database provided for the thermal assessment of a human at rest," *Biophys. Rev. Lett.* **5**(3), 129–151 (2010).
12. W.-F. Cheong, S. A. Prahl, and A. J. Welch, "A review of the optical properties of biological tissues," *IEEE J. Quantum Electron.* **26**(12), 2166–2185 (1990).
13. W. Star and J. Marijnissen, "Calculating the response of isotropic light dosimetry probes as a function of the tissue refractive index," *Appl. Opt.* **28**(12), 2288–2291 (1989).
14. J. De Poorter, "Noninvasive MRI thermometry with the proton resonance frequency method: study of susceptibility effects," *Magn. Reson. Med.* **34**(3), 359–367 (1995).
15. S. L. Jacques, "Optical properties of biological tissues: a review," *Phys. Med. Biol.* **58**(11), R37–R61 (2013).
16. B. Z. Fite et al., "Magnetic resonance thermometry at 7T for real-time monitoring and correction of ultrasound induced mild hyperthermia," *PLoS One* **7**(4), e35509 (2012).
17. C. W. Song, "Effect of local hyperthermia on blood flow and micro-environment: a review," *Cancer Res.* **44**, 4721–4730 (1984).
18. P. S. Tofts and A. G. Kermode, "Measurement of the blood-brain barrier permeability and leakage space using dynamic MR imaging," *Magn. Reson. Med.* **17**(2), 357–367 (1991).
19. B. Denis de Senneville, B. Quesson, and C. T. W. Moonen, "Magnetic resonance temperature imaging," *Int. J. Hyperthermia* **21**(6), 515–531 (2005).

**Tom J. L. Schreurs** is a PhD candidate in the Biomedical Engineering Department of Eindhoven University of Technology (TU/e), Eindhoven, The Netherlands. His research is focused on magnetic resonance imaging for optimization and evaluation of photodynamic therapy. After his bachelor's degree in electrical engineering, he received his master's degree in biomedical engineering from Eindhoven University of Technology in 2012.

**Robbert van Gorkum** is a PhD candidate at the Institute for Biomedical Engineering of the Swiss Federal Institute of Technology, Zürich. His research is focused on magnetic resonance imaging of the heart, with a specific attention to diffusion tensor imaging of the cardiac muscle fibers. After his bachelor's degree in biomedical engineering, he obtained his master's degree in 2015 from the same department at Eindhoven University of Technology.

**Xu U. Zhang** is a PhD candidate in the biomedical engineering and Physics Department of Academic Medical Center, Amsterdam, The Netherlands. His research focuses on the influence of external load on tissue optical properties using single fiber reflectance spectroscopy (SFR) and optical coherence tomography. After obtaining his bachelor's degree in electrical engineering, he received his master's degree in photonics from the Friedrich-Schiller-University Jena.

**Dirk J. Faber** is an assistant professor (Universitair Docent) of biomedical optics at the Department of Biomedical Engineering and Physics of the AMC, University of Amsterdam. He studied applied physics at the University of Twente in 2000 and graduated in "functional optical coherence tomography" at AMC in 2005. His research

interests are the physics of light–tissue interaction with specific application to cancer diagnosis.

**Ton G. van Leeuwen** is a full professor in biomedical physics and was appointed head of the Biomedical Engineering and Physics Department at the Academic Medical Center of the University of Amsterdam in 2008. His current research focuses on the physics of the interaction of light with tissue. He uses that knowledge for the development, introduction, and clinical evaluation of emerging optical imaging techniques for gathering quantitative functional and molecular information on tissues.

**Klaas Nicolay** was a full professor in biomedical NMR. He received his PhD from the University of Groningen in 1983. From 1999, he was appointed as professor at the Department of Biomedical Engineering at Eindhoven University of Technology, a position he held until his recent death. He published more than 350 papers on *in vivo* MR imaging and spectroscopy of biological tissues and the development of MR tools for noninvasive characterization of tissue status.

**Gustav J. Strijkers** is a full professor of preclinical and translational MRI in the Department of Biomedical Engineering and Physics at the Academic Medical Center of the University of Amsterdam, professor of biomedical NMR at Eindhoven University of Technology, and adjunct professor at the Translational and Molecular Imaging Institute, Mount Sinai School of Medicine, New York. His work focuses on the preclinical development and translation of novel MRI sequences for improved diagnostics and therapy monitoring of disease.